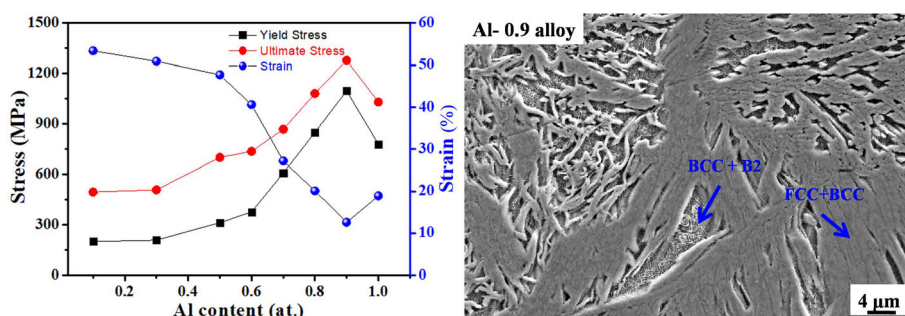


# Evolution of Microstructure and Mechanical Properties of As-Cast $\text{Al}_x\text{CrFe}_2\text{Ni}_2$ High-Entropy Alloys with Al Content



CHENGBIN WEI, LINWEI LI, YIPING LU, XINGHAO DU, and TONGMIN WANG

This study designed a series of low-cost  $\text{Al}_x\text{CrFe}_2\text{Ni}_2$  high-entropy alloys with different Al contents ( $x = 0.1-1.0$  at.) and investigated their microstructure and mechanical properties. The XRD analysis revealed that, with an increase in the Al content, their crystalline structures changed from the initial single face-centered cubic (FCC) one to FCC plus body-centered cubic (BCC) and ordered BCC (B2) structures. The tensile strength and hardness first increased and then dropped with increasing Al content related to the volume fraction of the FCC/BCC phase. At  $x = 0.9$ , the as-cast alloy containing 49.1 pct BCC phase exhibited the highest ultimate tensile strength of 1278 MPa with a 12.6 pct ductility. With an increase in the Al content, the alloy fracture mechanism changed from ductile fracture to brittle.



<https://doi.org/10.1007/s11661-021-06195-8>

© The Minerals, Metals & Materials Society and ASM International 2021

## I. INTRODUCTION

HIGH-ENTROPY alloys (HEAs), or multi-principal element alloys, have gained extensive attention due to the diversity in their composition, phase constitution, and promising mechanical properties.<sup>[1,2]</sup> Having a wide range of chemical compositions and phase constitutions, many HEAs have been designed with various excellent properties, such as high fracture toughness,<sup>[3]</sup> corrosion resistance,<sup>[4,5]</sup> mechanical properties,<sup>[6,7]</sup> radiation

stability,<sup>[8]</sup> wear resistance,<sup>[9]</sup> high-temperature performance,<sup>[10-12]</sup> and so on.

The microstructure and mechanical properties of HEAs are strongly affected by the added elements. In the  $\text{Al}_x\text{CoCrFeNi}(\text{Mn})$  alloy, the Al element promoted the formation of a body-centered cubic (BCC) structure and had a positive effect on the hardness.<sup>[13-15]</sup> Similarly, with an increase in the Al content, the structure of as-cast  $\text{CoCrFeMnNiAl}_x$  alloys changed from a single face-centered cubic (FCC) phase to a mixture of FCC + BCC and then to a single BCC phase. The mechanical properties also varied with the Al content.<sup>[14]</sup> Some studies explored the effect of Cr and Nb elements on the HEAs' phase stability and properties.<sup>[16-18]</sup> Cr at low concentrations acted as an FCC stabilizer, while Nb changed the HEAs' microstructure and properties.<sup>[17,18]</sup> The excellent performance was obtained by adjusting the content of such expensive elements as Nb, Mo, and Co.<sup>[18-20]</sup> It has been recently reported that increasing the content of Mo and decreasing that of Co in

CHENGBIN WEI, LINWEI LI, YIPING LU, and TONGMIN WANG are with the Key Laboratory of Solidification Control and Digital Preparation Technology (Liaoning Province), School of Materials Science and Engineering, Dalian University of Technology, Dalian, 116024, China. Contact emails: luyiping@dlut.edu.cn; tmwang@dlut.edu.cn XINGHAO DU is with the School of Materials Science and Engineering, Shenyang Aerospace University, Shenyang, 110136, China.

Manuscript submitted August 27, 2020; accepted February 3, 2021.

Article published online March 10, 2021

$\text{Fe}_{25}\text{Ni}_{25}\text{Co}_x\text{Mo}_y$  alloys resulted in the phase change from a single FCC to FCC + BCC + MoNi.<sup>[21]</sup> It was also revealed that Co atoms were energetically more stable in HCP structures<sup>[22]</sup> and had the most significant influence on the lattice parameter based on the first principle.<sup>[23]</sup> Also, increasing Co concentration could inhibit the formation of intermetallic phases in  $(\text{CrFeMnNi})_{100-x}\text{Co}_x$  alloys,<sup>[24]</sup> which was not conducive to the industrial application of HEAs. Hence, Dong *et al.*<sup>[25]</sup> designed a Co-free HEA composed of one FCC and two BCC phases. The element with lower valence electron concentration, such as Al, promoted the phase's stability.<sup>[26,27]</sup>

In this study, several  $\text{Al}_x\text{CrFe}_2\text{Ni}_2$  ( $x = 0.1-1.0$ ) were fabricated. The effect of different Al contents on their microstructure and mechanical properties were examined, and a correlation between the FCC/BCC phases, microstructure, and mechanical properties was discussed in detail.

## II. MATERIALS AND METHODS

The as-cast alloys  $\text{Al}_x\text{CrFe}_2\text{Ni}_2$  ( $x = 0.1, 0.3, 0.5, 0.6, 0.7, 0.8, 0.9, \text{ and } 1.0$ , denoted as Al- $x$ ) were prepared with compact vacuum induction melting equipment in Ar atmosphere, using high-purity (>99.95 wt pct) Al, Cr, Fe and Ni metal particles. Then the molten metal was poured into a rectangular module, and about 110 g ingot was obtained.

The as-cast samples were sectioned and polished following the standard metallographic procedure. Next, they were etched with a solution of  $\text{H}_2\text{SO}_4 + \text{HNO}_3$  with a volume ratio of 3:1. The microstructure was examined *via* an Olympus (GX51) optical microscopy (OM) and scanning electron microscopy (SEM, SUPARR 55) equipped with energy-dispersive spectroscopy (EDS). The phase morphology of polished samples was studied *via* a JXA-8530F PLUS electron probe microscope (EPMA). The elemental compositions were experimentally determined by SEM-EDS and EPMA. Based on EPMA data, each alloy phase's volume fraction was estimated using the ImageJ software by the grid method from more than five different areas. The grain size was measured by the linear intercept method based on the OM data.<sup>[28]</sup> The crystalline structures of the ingots were analyzed *via* X-ray diffraction (XRD). The XRD measurements were conducted on an Empyrean machine (PANalytical B.V.) with  $\text{Cu-K}\alpha$  radiation at 40 kV and 30 mA. The scanning range was between 30 deg and 100 deg ( $2\theta$ ) with a step size of  $6^\circ/\text{min}$ .

Transmission electron microscopy (TEM) observations were conducted on a JEM-F200 operated at 200 kV. TEM samples were mechanically thinned to 30  $\mu\text{m}$ , punched to disks of 3 mm in diameter, and then thinned by twin-jet electro-polishing using a mixture of 7 vol pct perchloric acid and 93 vol pct alcohol at a temperature of 243 K with 25 V.

The tensile tests were performed *via* an Instron 5569 test machine with a strain rate of  $10^{-3} \text{ s}^{-1}$  at room temperature. Dog-bone-shaped specimens for tensile

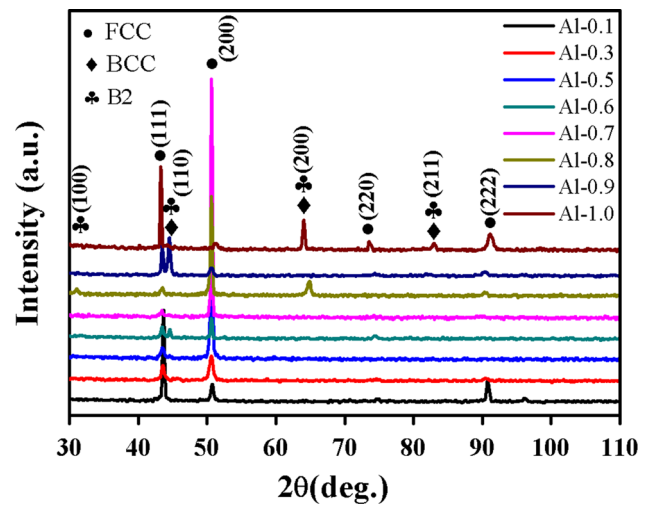


Fig. 1—XRD patterns of the as-cast  $\text{Al}_x\text{CrFe}_2\text{Ni}_2$  alloys.

tests (with a gage length of 12.5 mm, a width of 3 mm, and a thickness of 2 mm) were cut from the as-cast alloys by electric discharging machining (EDM). Their surfaces were ground to 1500 grit using SiC paper. Three tensile specimens were tested to ensure the reproducibility of the results. The details of the test method can be found elsewhere.<sup>[29]</sup> Hardness measurements were conducted on a Vickers hardness tester (MH-50) with a load of 500 g applied for 15 seconds. Before the hardness testing, the samples' surface was first ground down to 2000 grits and polished to remove any scratches. Each sample was tested at least in ten different points to obtain an average value of hardness.

## III. RESULTS

### A. Microstructural Evolution

Figure 1 shows the XRD patterns of the as-cast alloys with different Al contents. The crystal structure transitioned from a single FCC to FCC + BCC phases with the Al element's addition. At  $x$  values of 0.1 and 0.3, the diffraction peaks indicated the presence of only a single FCC phase. Scarce precipitates in the Al-0.3 alloy were also revealed after closer examinations, as discussed below. Minor diffraction peaks of the BCC (near 45 deg) phase started to appear in the Al-0.5 alloy. The diffraction peak intensity of the BCC phase increased with the Al content. For the Al-0.8 alloy, the diffraction peak was identified as B2 phases near 30 deg. For the Al-0.9 and Al-1.0 alloys, the alloys exhibited a mixture of FCC, BCC, and B2 crystal structures. The Al-1.0 alloy exhibited a mixture of FCC, disordered BCC, and B2 crystal structures.<sup>[25]</sup>

Figure 2 illustrates microstructural evolution in the as-cast  $\text{Al}_x\text{CrFe}_2\text{Ni}_2$  alloys. At the Al content not exceeding 0.1, as shown in Figure 2(a), the alloy presented a single-solid-solution structure with a grain size of  $\sim 272 \mu\text{m}$ . With an increase in Al content, the alloy's grain size dropped to 178  $\mu\text{m}$  (in Al-0.3 alloy). Besides, scarce precipitations were observed in the

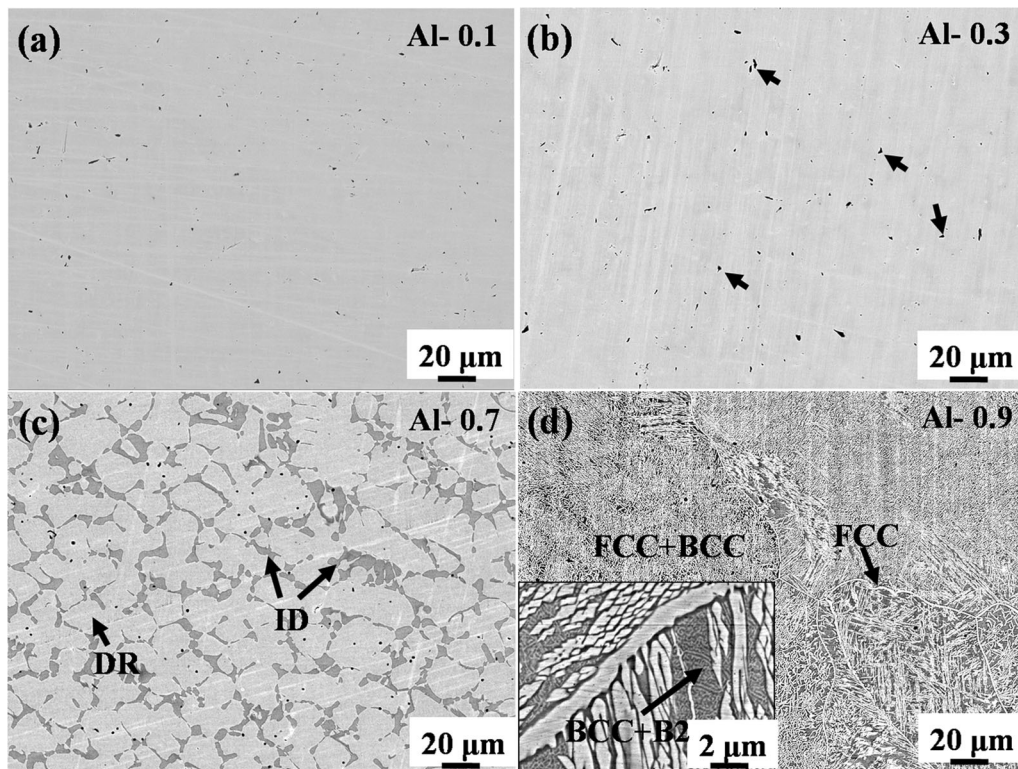


Fig. 2—The microstructure of as-cast  $\text{Al}_x\text{CrFe}_2\text{Ni}_2$  alloys: (a) Al-0.1 alloy; (b) Al-0.3 alloy; (c) Al-0.7 alloy; and (d) Al-0.9 alloy. The inset image of the Al-0.9 alloy in (d) has a higher magnification.

microstructure, as shown in Figure 2(b) marked with black arrows. However, their fractions were too small to be detected by the XRD, which revealed only a single-phase structure, as shown in Figure 1. At higher Al content, typical cast dendritic (DR) and interdendritic (ID) structures were observed. As soon as the Al content reached 0.7, the ID structures became coarser (Figure 2(c)). With further increase in the Al content, partial DR structures were transformed into lamellar ones. The volume of ID structures was increased, as seen in the inset of Figure 2(d) with a higher magnification of the Al-0.9 alloy image. The microstructure of ID regions featured typical characteristics of a spinodal transformation, which could be decomposed into two coherent phases.<sup>[30]</sup> According to these alloys' XRD pattern, the single-solid-solution and DR structures corresponded to the FCC solid-solution phase and the ID structure to BCC/B2 phases.

Figure 3 presents high-magnified SEM images of these alloys. At Al content of 0.3, except for FCC matrix, minor precipitations are embedded in the matrix, as shown in Figure 3(a). In Al-0.5 and Al-0.7 alloys, precipitates with a diameter of less than 100 nm were embedded in the ID region (Figures 3(b) and (c)). The honeycomb-like structures were formed due to the etching-induced loose precipitations. The chemical compositions of alloy's different regions were assessed *via* EDS and EPMA, as shown in Table I. At Al content above 0.5, the DR structures were enriched with Fe, Cr, and Ni elements, while ID structures were enriched with Al and Ni elements. In general, increased contents of Al

and Ni formed B2 phases, while those of Cr, Fe, and Ni formed FCC phases.<sup>[25]</sup>

Figures 4(a) through (c) present the bright-field (BF) TEM micrograph and corresponding selected area electron diffraction (SAED) patterns of Al-0.5 alloy. They confirmed that the ID regions corresponded to the B2 phase, while the matrix was composed of the FCC phase. At  $x < 0.5$ , the matrix of  $\text{Al}_x\text{CrFe}_2\text{Ni}_2$  alloys was the FCC phase. With an increase in Al content ( $x$ ), the respective structure comprised FCC, BCC, and decomposition microstructure (BCC + B2). The FCC and BCC phases were formed directly from the melt, and the spinodal decomposition microstructure was generally formed *via* the B2 phase (ID) decomposition.<sup>[30]</sup> The above findings were consistent with the XRD results. At  $x > 0.8$ , the laminated BCC and FCC phases, denoted in Figures 3(d) through (f) by white and black arrows, respectively, appeared in the alloy. Figures 4(d) through (f) present the BF TEM micrograph and corresponding SAED patterns of the Al-0.9 alloy. They corroborated the earlier finding that the microstructure was composed of FCC, BCC, and B2 phases.

Figure 5 depicts the volume fraction of the BCC phase (BCC and B2 phases) *vs* Al content estimated *via* the EPMA data processed by the grid method for more than five different areas. With an increase in the Al content, the BCC phase's volume fraction first increased and then dropped. Its maximum value of about 49 pct was observed at  $x = 0.9$ , further dropping to 41 pct at  $x = 1.0$  (*i.e.*, in the Al-1.0 alloy).

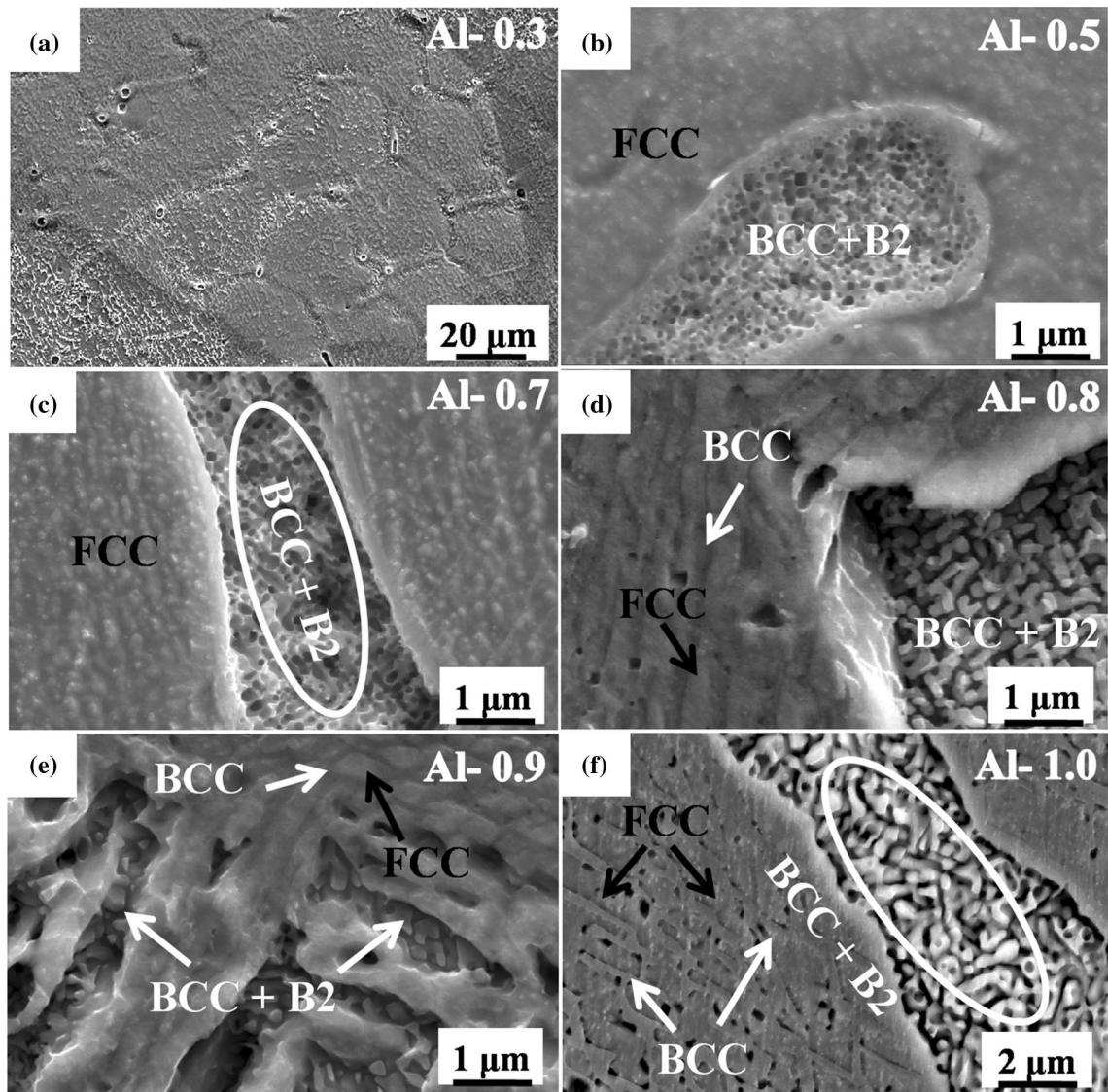


Fig. 3—High-magnification SEM images of as-cast  $\text{Al}_x\text{CrFe}_2\text{Ni}_2$  alloys: (a) Al-0.3 alloy; (b) Al-0.5 alloy; (c) Al-0.7 alloy; (d) Al-0.8 alloy; (e) Al-0.9 alloy; and (f) Al-1.0 alloy.

### B. Mechanical Properties

Figure 6(a) shows the engineering stress-strain curves of as-cast  $\text{Al}_x\text{CrFe}_2\text{Ni}_2$  alloys with different Al contents. With an increase in the Al content, the tensile fracture strength first increased and then dropped. Meanwhile, the tensile ductility variation followed the opposite trend. At  $x$  values not exceeding 0.3, the tensile engineering stress-strain curves of Al-0.1 and Al-0.3 alloys were similar. These alloys had the maximum ductility of 50 pct, while their yield and ultimate tensile strengths were only about 200 and 500 MPa, respectively. At  $x > 0.5$ , the strains dropped, and both yield and ultimate tensile strength increased sharply. The maximum yield and ultimate tensile strengths of the Al-0.9 alloy were 1097 and 1278 MPa, respectively. However, the ductility was only 12.6 pct. At  $x = 1.0$ , the alloy's yield and ultimate tensile strengths dropped to 780 and 1031 MPa, while the ductility slightly

increased to 18.9 pct. These patterns were contradictory to the findings of authors,<sup>[14]</sup> which implied that the yield and ultimate strengths increased sharply and ductility dropped significantly with an increase in the Al content in  $(\text{FeCoNiCrMn})_{100-x}\text{Al}_x$  alloys. Figure 6(b) presents the mechanical properties of as-cast alloys with different Al contents.

Figure 7(a) depicts the hardness variation with Al contents. A positive linear correlation is observed in a certain range. At the Al content not exceeding 0.3, the single FCC structure's hardness showed no obvious change, and the lowest hardness was about 135 HV. Similar to strength, hardness slightly increased with the Al content increases from 0.5 to 0.6. However, at  $x > 0.7$ , the hardness increased dramatically, reaching a maximum value of 349 HV at  $x = 0.9$ . At  $x = 1.0$ , the hardness dropped to 283 HV, exceeding the value 274 HV in Al-0.8. The hardness also positively correlated with the volume fraction of BCC phases, as shown in

**Table I. Chemical Composition of Different Regions in As-Cast Al<sub>x</sub>CrFe<sub>2</sub>Ni<sub>2</sub> Alloys**

Alloy	Region	Element (at. pct)			
		Al	Cr	Fe	Ni
$x = 0.1$	FCC	2.06	20.68	38.43	38.83
$x = 0.3$	FCC	6.53	18.65	37.40	37.42
$x = 0.5$	FCC	9.65	18.64	34.39	37.32
	BCC	24.23	10.90	19.94	44.93
$x = 0.6$	FCC	10.89	18.49	38.37	32.25
	BCC	22.23	13.40	23.59	40.78
$x = 0.7$	FCC	9.93	18.68	39.47	31.92
	BCC	25.43	13.45	23.07	38.05
$x = 0.8$	FCC	10.10	19.07	40.06	30.77
	BCC	24.69	9.90	22.18	43.23
$x = 0.9$	FCC	9.25	19.86	38.27	32.62
	BCC	23.67	12.39	24.59	39.35
$x = 1.0$	FCC	9.97	20.16	41.68	28.19
	BCC	24.04	13.10	26.42	36.44

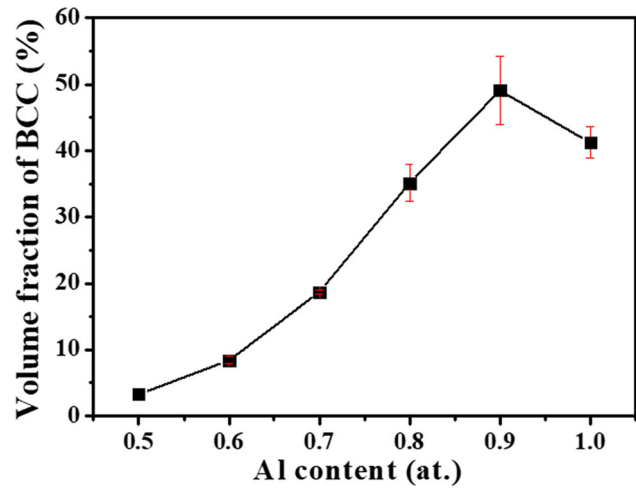


Fig. 5—The volume fraction of (BCC + B2) phases vs Al content.

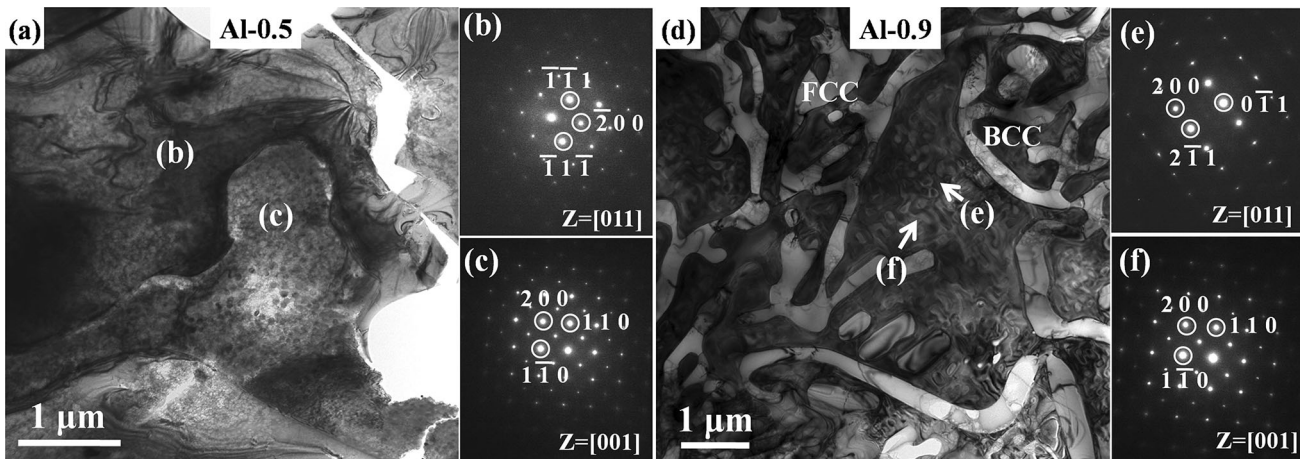


Fig. 4—BF TEM image with the corresponding SAED patterns of Al-0.5 (a through c) and Al-0.9 (d through f) alloys: (a) BF image of Al-0.5 alloy; (b) SAED pattern of region (b) in (a) confirms the FCC phase identification; (c) SAED pattern of region (c) in (a) confirms the B2 phase identification; (d) BF image of Al-0.9 alloy; (e) SAED pattern of region (e) in (d) confirms the BCC phase identification; (f) SAED pattern of region (f) in (d) confirms the B2 phase identification.

Figure 7(b). These results strongly indicated that the BCC/B2 phases were the main hardening constituents of these alloys.

## IV. DISCUSSION

### A. Effect of Al Content on Microstructural Evolution

In steels and many reported HEAs systems, Al was considered beneficial for forming the BCC phase.<sup>[13,31,32]</sup> Figure 5 shows a close linear relationship between the Al content and the BCC phase fraction at  $x < 0.9$ . Several parameters were proposed/adopted in previous studies to predict the phase presence and its stability in HEAs. Thus, Guo *et al.* proposed to use a valence electron concentration (VEC), which calculated as follows:<sup>[33,34]</sup>

$$VEC = \sum_{i=1}^n c_i(VEC)_i, \quad [1]$$

where  $c_i$  is the atomic percentage, and  $(VEC)_i$  is VEC of the  $i$ th element. They reported that at  $VEC > 8$ , the single FCC phases were stable, while at VEC in the range from 6.87 and 8, the FCC and BCC phases coexisted in the alloys. The VEC values for alloys under study were calculated *via* Eq. [1] and plotted in Figure 8: they nearly linearly decreased with the Al content ( $x$ ). At  $x < 0.3$ , alloys had  $VEC > 8$ . At  $x = 1.0$ , VEC's value dropped to 7.5. This study's phase composition changed from a single FCC to FCC + BCC + B2 phase, which was consistent with the XRD and SEM results.

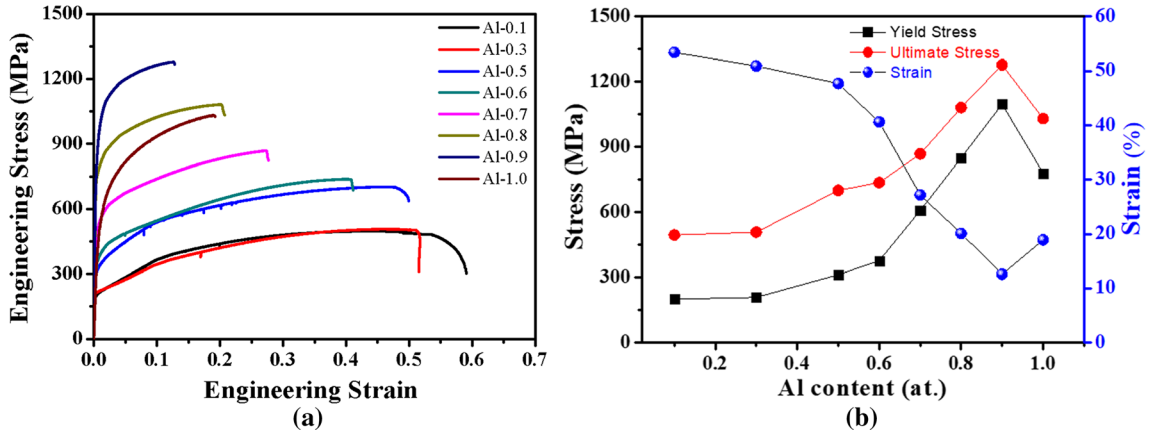


Fig. 6—Mechanical properties of as-cast  $\text{Al}_x\text{CrFe}_2\text{Ni}_2$  alloys. (a) engineering stress-strain curves; (b) ultimate tensile strength, yield strength, and tensile ductility vs Al content.

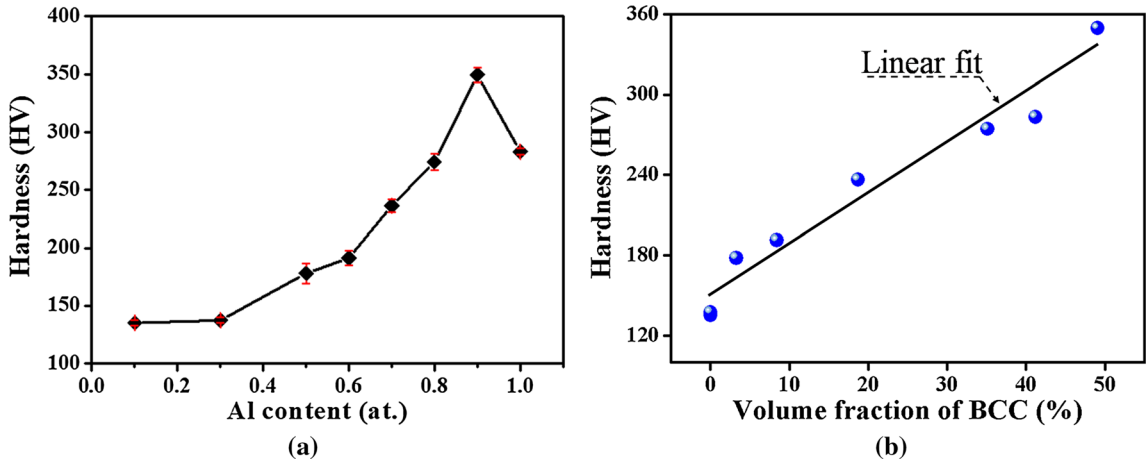


Fig. 7—Hardness vs Al content (a) and volume fraction of BCC phases (b) in the as-cast alloys. The BCC phases contained BCC and B2 phases.

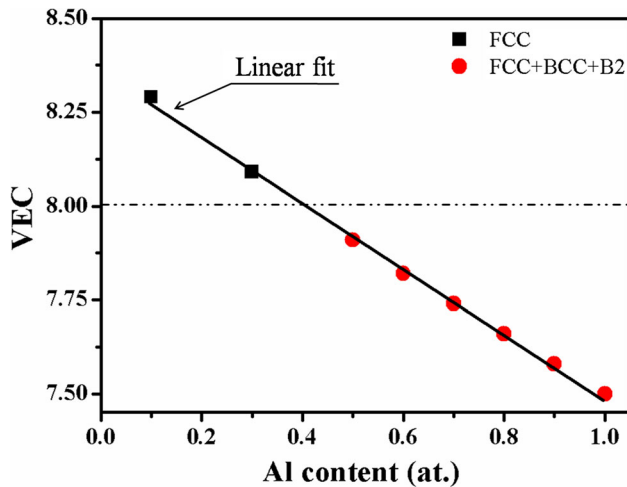


Fig. 8—A nearly linear relationship between VEC and Al content in the as-cast alloys under study.

Several other physical parameters have been alternatively used to predict structural stability and phase formation.<sup>[33–36]</sup> Zhang *et al.*<sup>[36]</sup> proposed a criterion for

achieving solid-solution phases in HEAs, using two parameters, namely mixing enthalpy ( $\Delta H_{\text{mix}}$ ) and mean square deviation of the atomic radii difference ( $\delta$ ):

$$\Delta H_{\text{mix}} = 4 \sum_{i=1, i \neq j}^n \Delta H_{ij}^{\text{mix}} c_i c_j, \quad [2]$$

$$\delta = \sqrt{\sum_{i=1}^n c_i (1 - r_i / \bar{r})^2}, \quad [3]$$

where  $\Delta H_{ij}^{\text{mix}}$  is the enthalpy of mixing between the  $i$ th and  $j$ th elements,  $c_i$  is the molar ratio; and  $r_i$  is the  $i$ th element's atomic radius. They reported a random solid solution formed within the ranges of  $-15 \text{ kJ/mol} \leq \Delta H_{\text{mix}} \leq 5 \text{ kJ/mol}$  and  $1 \text{ pct} < \delta < 6 \text{ pct}$ . In the present study,  $\Delta H_{ij}^{\text{mix}}$  and  $\delta$  ranges from  $-11.12$  to  $-4.84 \text{ kJ/mol}$  and from  $2.1 \text{ pct}$  to  $5.4 \text{ pct}$ , respectively, were determined. Thus, the phases in the present study almost coincided with those envisaged by the above criterion. According to the above theoretical predictions, the volume fraction of BCC (BCC + B2) phases should increase with the Al content. However, the volume

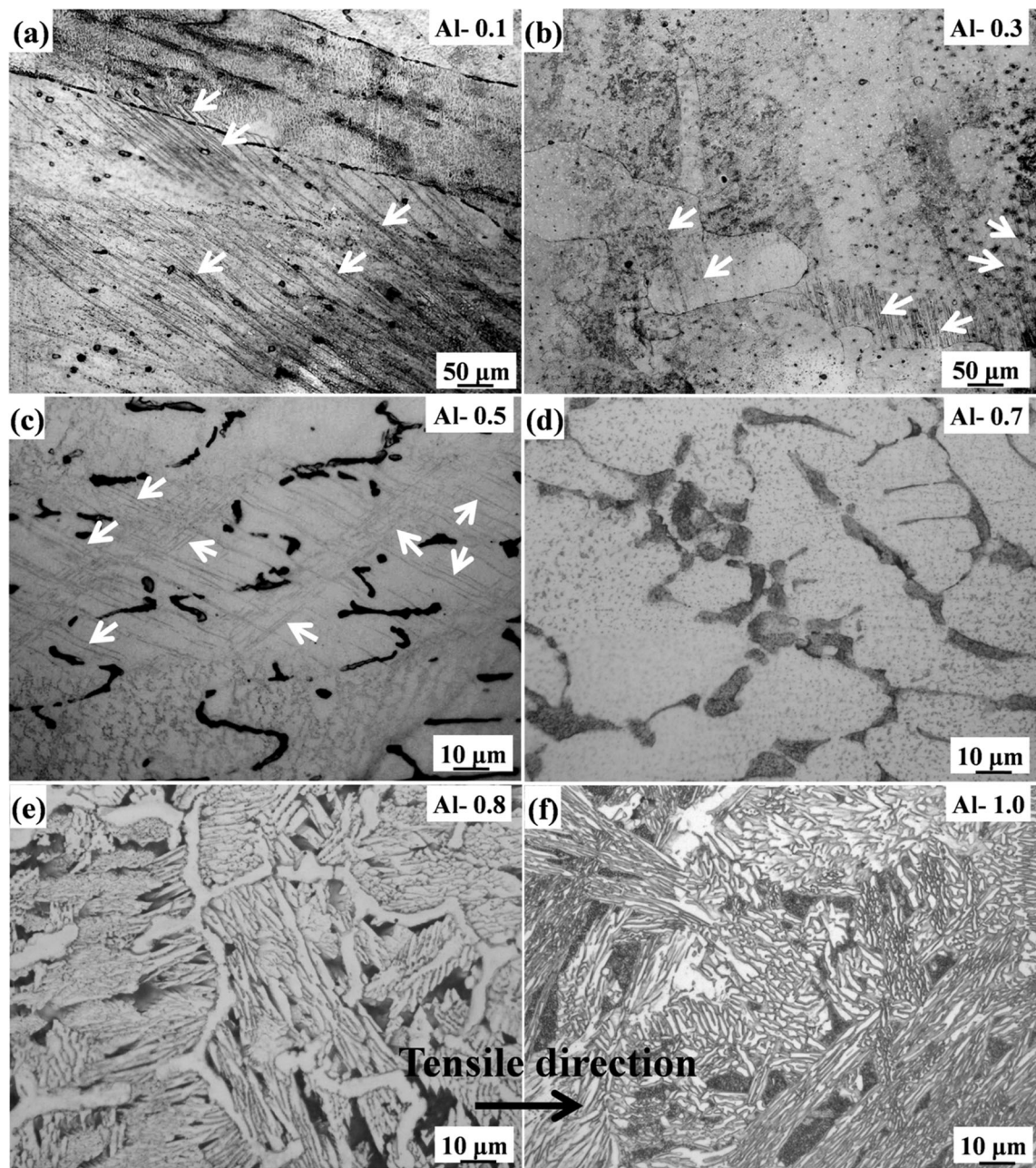


Fig. 9—Optical micrographs of the lateral surface in the vicinity of the fracture in tensile specimens: (a) Al-0.1 alloy; (b) Al-0.3 alloy; (c) Al-0.5 alloy; (d) Al-0.7 alloy; (e) Al-0.8 alloy and (f) Al-1.0 alloy.

fraction of the BCC phase decreased in the Al-1.0 alloy. This abnormal phenomenon needs to be investigated in subsequent studies.

### B. Effect of Al Content on Mechanical Properties

The results obtained imply that the mechanical properties of the alloys under study strongly depend on their microstructure. At  $x < 0.1$ , the alloy's phase composition was a single FCC phase with excellent ductility but low strength. As the Al content was slightly increased, the solid-solution strengthening was insignificant, and the mechanical properties were enhanced

slightly. Compared with the Al-0.3 alloy, the Al-0.5 and Al-0.6 ones showed higher strength and a lower ductility because many hard BCC and B2 phases were formed in the grain boundaries with an increase in the Al content and served as hard phases. During the process of tensile deformation, these hard BCC and B2 phases effectively improved the alloy strength. Meanwhile, stress concentration also occurred around these hard phases, easily forming microcracks with increased tensile stresses. The ductility decreased sharply in the Al-0.7 alloy. Figure 9 presents the lateral surface in the vicinity of the fracture after tensile tests. Deformation twins marked by white arrows in Figures 9(a) through (c) were observed in the

tensile specimens at  $x \leq 0.5$  but were hard to detect in Al-0.7, Al-0.8, and Al-1.0 alloys, as shown in Figures 9(d) through (f). The critical stress for twinning increased with grain size reduction.<sup>[36–38]</sup> If the grain size exceeded a threshold value and the concentrated stress was also larger than the critical stress for twinning, many twins were generated with an increase in tensile stress. In this study, the grain size varied from  $\sim 272 \mu\text{m}$  in Al-0.1 alloy to about  $49 \mu\text{m}$  in Al-0.5 one. At higher  $x$  values, the critical stresses for twinning were much larger, and the concentrated stresses were insufficient for forming twins in the alloys. Besides, the stacking fault energy (SFE) has been found to promote the occurrence of twinning.<sup>[33]</sup> The SFE value usually increases with Al content.<sup>[39]</sup> Besides dislocation slips, the twinning mechanism also facilitates the alloy deformation. The absence of a twinning-induced plasticity mechanism is also known to reduce the alloy ductility. In general, mechanical properties show a conventional strength ductility trade-off behavior with increasing Al content. At  $x = 1.0$ , the decrease in strength and hardness was related to the low volume fraction of BCC phases. Although the latter was higher in the Al-1.0 alloy than in Al-0.8 one, their strength and ductility followed opposite trends. This abnormal result might be related to different volume fractions of mixture phases. The volume fraction of BCC phases in the Al-1.0 alloy was larger than that in the Al-0.8 alloy. However, BCC phases in the Al-0.8 alloy were thinner than those in the Al-1.0 alloy (Figures 3(d) and (f)). Smaller-sized phases possessed higher interface areas. A large number of dislocations first occurred in the FCC phase, and then the dislocation slip was pinned at the FCC/BCC (B2) boundaries during the tensile tests. The larger the interface area, the stronger the impeding effect and the dislocation-accumulation capability at the phase boundaries (PBs). The PBs' impeding effect resulted in higher strength and ductility of the Al-0.8 alloy, as compared to Al-1.0 one.<sup>[13]</sup>

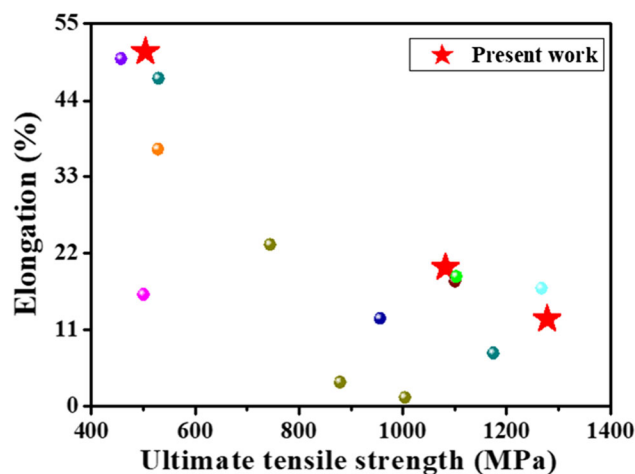


Fig. 10—Elongation vs ultimate tensile strength of some as-cast HEAs. Red stars correspond to this study's data, while other reference data are listed in Table S-I of the supplementary electronic material (Color figure online).

Figure 10 allows one to visually compare the elongation and ultimate tensile strength values in some as-cast HEAs prepared. The reference data are listed in Table S-I (refer to Electronic Supplementary Material). The location of current alloys marked with red stars indicates that the respective properties outperform those of most reported as-cast HEAs, being only slightly inferior to as-cast  $\text{Ni}_{30}\text{Co}_{30}\text{Cr}_{10}\text{Fe}_{10}\text{Al}_{18}\text{W}_2$  alloy.

### C. Fracture Mechanism of the As-Cast $\text{Al}_x\text{CrFe}_2\text{Ni}_2$ Alloys

The fracture surface morphologies of the as-cast alloys are presented in Figure 11 to clarify correlation between the microstructure, mechanical properties, fracture mechanisms and the Al content. As seen in Figure 11(a), multiple dimples of different sizes are widely distributed in the fracture surface of the Al-0.1 alloy, and no cracks are observed. The corresponding lateral microstructure exhibits an intercrystalline fracture (IF) with a zigzag shape, as displayed in Figure 11(b). The presence of these dimples directly correlates with its high ductility. At  $x = 0.6$ , a few shallow dimples (white arrows), tear ridges (TRs), cleavage planes (CPs), and smooth grain boundaries GBs/PBs can be observed on the fracture surface, as shown in Figure 11(c). The lateral microstructure exhibits the IF with a fine arc and a few transgranular fractures (TFs) (Figure 11(d)). However, these TRs and dimples still contribute to ductility. Hence, the main fracture mechanism in the Al-0.6 alloy is cleavage fracture. At  $x = 0.7$ , the fracture surface has a typical cleavage fracture (Figure 11(e)). The lateral microstructure exhibits an IF morphology (Figure 11(f)). Besides GBs/PBs, some secondary cracks (SCs) are distributed at the fracture surface. This implies that shear cracks propagate through the FCC and BCC phases, followed by the specimen fracture. At  $x \geq 0.8$ , the fracture morphology possesses typical cleavage and quasi-cleavage fracture characteristics (Figures 11(g) and (h)). These results indicate that the fracture mechanism changes from ductile fracture to brittle one with an increase in the Al content. However, no cracks at the PBs are observed (fracture surfaces of other alloys are displayed in Figure S-1, refer to Electronic Supplementary Material). Thus, cracks can nucleate at the FCC/BCC PBs and then propagate through the boundaries, leading to the eventual fracture.<sup>[40]</sup>

## V. CONCLUSIONS

In this study, the effect of Al content on the microstructure evolution and mechanical properties of  $\text{Al}_x\text{CrFe}_2\text{Ni}_2$  ( $x = 0.1, 0.3, 0.5, 0.6, 0.7, 0.8, 0.9$ , and  $1.0$ ) alloys was investigated. The results obtained made it possible to draw the following conclusions:

1. A single FCC structure was formed at Al content ( $x$ ) below 0.1. With an increase in the Al content, the crystalline structures changed to FCC + BCC and B2 phases. The spinodal decomposed structure



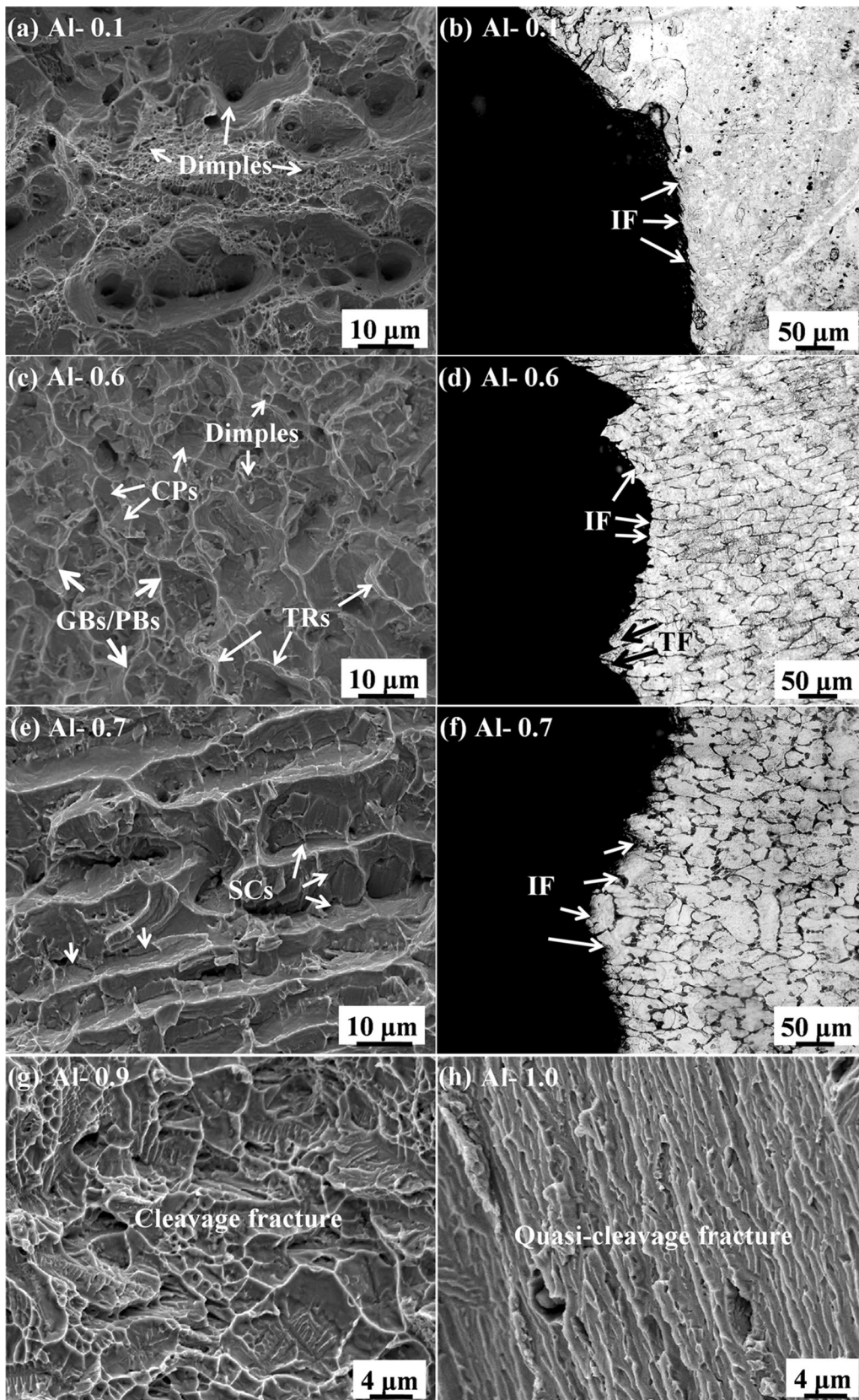


Fig. 11—Fracture morphology and lateral microstructure after tensile deformation of as-cast Al- $x$  alloys: Al-0.1 (*a, b*); Al-0.6 (*c, d*); Al-0.7 (*e, f*); Al-0.9 (*g*) and Al-1.0 (*h*).

was derived from the decomposition of the B2 phase.

- The volume fraction of BCC and B2 phases first increased and then decreased with the Al content. Strength and hardness were strongly dependent on the volume fraction of BCC phases. Generally, the mechanical properties showed a strength ductility trade-off behavior. The Al-0.9 alloy contained a 49.1 pct BCC phase and exhibited the highest ultimate strength of 1278 MPa with 12.6 pct ductility. The hardness reached a maximum of 349 HV.
- At  $x = 1.0$ , the alloy exhibited abnormal trends of microstructure and mechanical properties, with a sharp drop in the BCC volume fraction and strength values. This can be related to the different volume fraction of mixture phases and interface areas.
- With an increase in the Al content, the fracture mechanism changed from ductile fracture to brittle one, which is confirmed by the respective variation of mechanical properties.

#### ACKNOWLEDGMENTS

This work was supported by the National Key Research and Development Program of China (Grant No. 2017YFA0403803), the Special Fund for Research on National Major Research Instrument (Grant No. 51927801), the National Key Research and Development Program of China (Nos. 2019YFA0209901 and 2018YFA0702901), the fund of the State Key Laboratory of Solidification Processing in NWPU (Grant No. SKLSP201902), the Liao Ning Revitalization Talents Program (XLYC1807047), the National MCF Energy R&D Program (Project No. 2018YFE0312400), and the Fund of Science and Technology on Reactor Fuel and Materials Laboratory (STRFML-2020-04).

#### SUPPLEMENTARY INFORMATION

The online version contains supplementary material available at <https://doi.org/10.1007/s11661-021-06195-8>.

#### REFERENCES

- J.W. Yeh, S.K. Chen, S.J. Lin, J.Y. Gan, T.S. Chin, T.T. Shun, C.H. Tsau, and S.Y. Chang: *Adv. Eng. Mater.*, 2004, vol. 6, pp. 299–303.
- B. Cantor, I.T.H. Chang, P. Knight, and A.J.B. Vincent: *Mater. Sci. Eng. A*, 2004, vols. 375–377, pp. 213–18.
- B. Gludovatz, A. Hohenwarter, D. Catoor, E.H. Chang, E.P. George, and R.O. Ritchie: *Science*, 2014, vol. 345, pp. 1153–58.
- H. Luo, Z. Li, A.M. Mingers, and D. Raabe: *Corros. Sci.*, 2018, vol. 134, pp. 131–39.
- M.C. Gao, J.W. Yeh, P.K. Liaw, and Y. Zhang: *High-entropy alloys: Fundamentals and Applications*, 1st ed., Springer, Cham, 2016, pp. 248–59.
- XH Du, WP Li, HT Chang, T Yang, GS Duan, BL Wu, JC Huang, FR Chen, CT Liu, WS Chuang, Y Lu, ML Sui, and EW Huang: *Nat. Commun.*, 2020, vol. 11, p. 2390.
- P. Sathiyamoorthi and H.S. Kim: *Prog. Mater. Sci.*, 2020, <https://doi.org/10.1016/j.pmatsci.2020.100709>.
- YP Lu, HT Huang, XZ Gao, CL Ren, J Gao, HZ Zhang, SJ Zheng, QQ Jin, YH Zhao, CY Lu, TM Wang, and TJ Li: *J. Mater. Sci. Technol.*, 2019, vol. 35, pp. 369–73.
- Y. Zhang, T.T. Zuo, Z. Tang, M.C. Gao, K.A. Dahmen, P.K. Liaw, and Z.P. Lu: *Prog. Mater. Sci.*, 2014, vol. 61, pp. 1–93.
- ON Senkov, S Gorsse, and DB Miracle: *Acta Mater.*, 2019, vol. 175, pp. 394–405.
- O.N. Senkov, A.L. Pilchak, and S.L. Semiatin: *Metall. Mater. Trans. A*, 2018, vol. 49, pp. 2876–92.
- H.T. Jeong, H.K. Park, K. Park, T.W. Na, and W.J. Kim: *Mater. Sci. Eng., A*, 2019, vol. 756, pp. 528–37.
- W. Wang, W. Wang, S. Wang, Y. Tsai, C. Lai, and J. Yeh: *Intermetallics*, 2012, vol. 26, pp. 44–51.
- J.Y. He, W.H. Liu, H. Wang, Y. Wu, X.J. Liu, T.G. Nieh, and Z.P. Lu: *Acta Mater.*, 2014, vol. 62, pp. 105–13.
- A. Asabre, A. Kostka, O. Stryzhyboroda, J. Pfetzing-Micklich, U. Hecht, and G. Laplanche: *Mater. Des.*, 2019, vol. 184, p. 108201.
- F Meng, J Qiu, and I Baker: *Mater. Sci. Eng. A*, 2013, vol. 586, pp. 45–52.
- X. Jin, Y. Liang, J. Bi, and B. Li: *J. Alloys Compd.*, 2019, vol. 798, pp. 243–48.
- U. Sunkari, S.R. Reddy, K.S. Athira, S. Chatterjee, and P.P. Bhattacharjee: *Mater. Sci. Eng. A*, 2020, vol. 793, p. 139897.
- K.S. Ming, X.F. Bi, and J. Wang: *Scripta Mater.*, 2017, vol. 137, pp. 88–93.
- D.X. Wei, X.Q. Li, W.C. Heng, Y. Koizumi, F. He, W.M. Choi, B.J. Lee, H.S. Kim, H. Kato, and A. Chiba: *Mater. Res. Lett.*, 2019, vol. 7, pp. 82–88.
- N. Liu, W. Ding, X.J. Wang, C. Mu, J.J. Du, and L.X. Liu: *Metall. Mater. Trans. A*, 2020, vol. 51A, pp. 2990–97.
- Y. Koizumi, T. Nukaya, S. Suzuki, S. Kurosu, Y. Li, H. Matsumoto, K. Sato, Y. Tanaka, and A. Chiba: *Acta Mater.*, 2012, vol. 60, pp. 2901–15.
- C. Niu, A.J. Zaddach, C.C. Koch, and D.L. Irving: *J. Alloy. Compd.*, 2016, vol. 672, pp. 510–20.
- Z.G. Zhu, K.H. Ma, X. Yang, and C.H. Shek: *J. Alloys Compd.*, 2017, vol. 695, pp. 2945–50.
- Y. Dong, X.X. Gao, Y.P. Lu, T.M. Wang, and T.J. Li: *Mater. Lett.*, 2016, vol. 169, pp. 62–64.
- M. Ogura, T. Fukushima, R. Zeller, and P.H. Dederichs: *J. Alloys Compd.*, 2017, vol. 715, pp. 454–59.
- S. Elkatatny, M.A.H. Gepreel, A. Hamada, K. Nakamura, K. Yamanaka, and A. Chiba: *Mater. Sci. Eng. A*, 2019, vol. 759, pp. 380–90.
- ASTM E112-13, Standard test methods for determining average grain size, West Conshohocken, PA(US), *ASTM International*, February 2014.
- ASTM E8/E8M-13a, Standard test methods for tension testing of metallic materials, West Conshohocken, PA(US), *ASTM International*, May 2015.
- L.J. Santodonato, Y. Zhang, M. Feygenon, C.M. Parish, M.C. Gao, R.J.K. Weber, J.C. Neuefeind, Z. Tang, and P.K. Liaw: *Nat. Commun.*, 2015, vol. 6, pp. 5964–76.
- H.K.D.H. Bhadeshia and R.W.K. Honeycombe: *Steels: microstructure and properties*, 3rd ed., Elsevier, Oxford, 2006, pp. 71–93.
- K. Zhang and Z. Fu: *Intermetallics*, 2012, vol. 22, pp. 24–32.
- S. Guo and C.T. Liu: *Prog. Nat. Sci.: Mater. Int.*, 2011, vol. 21, pp. 433–46.
- S. Guo, C. Ng, J. Lu, and C.T. Liu: *J. Appl. Phys.*, 2011, vol. 109, p. 103505.
- X. Yang and Y. Zhang: *Mater. Chem. Phys.*, 2012, vol. 132, pp. 233–38.
- Y. Zhang, Y.J. Zhou, J.P. Lin, G.L. Chen, and P.K. Liaw: *Adv. Eng. Mater.*, 2008, vol. 10, pp. 534–38.

37. I. Gutierrez-Urrutia, S. Zaefferer, and D. Raabe: *Mater. Sci. Eng. A*, 2010, vol. 527, pp. 3552–60.
38. E. El-Danaf, S.R. Kalidindi, and R.D. Doherty: *Metall. Mater. Trans. A*, 1999, vol. 30A, pp. 1223–33.
39. S. Hong, S.Y. Shin, H.S. Kim, S. Lee, S.K. Kim, K.G. Chin, and N.J. Kim: *Metall. Mater. Trans. A*, 2012, vol. 43A, pp. 1870–83.
40. X.Z. Gao, Y.P. Lu, B. Zhang, N.N. Liang, G.Z. Wu, G. Sha, J.Z. Liu, and Y.H. Zhao: *Acta Mater.*, 2017, vol. 141, pp. 59–66.

**Publisher's Note** Springer Nature remains neutral with regard to jurisdictional claims in published maps and institutional affiliations.